Effective heat dissipation in an adiabatic near-field transducer for HAMR

CHUAN ZHONG,[1,2] PATRICK FLANIGAN,[1,2] NICOLÁS ABADÍA,[1,2] FRANK BELLO,[1,2] BRIAN D. JENNINGS,[1,2] GWENAEL ATCHESON,[1,2] JING LI,[2,3] JIAN-YAO ZHENG,[1,2] JING JING WANG,[1,2] RICHARD HOBBS,[2,3] DAVID MCCLOSKEY,[1,2] AND JOHN F. DONEGAN[1,2,*]

[1]School of Physics, Trinity College Dublin, Dublin 2, Ireland
[2]Centre for Research on Adaptive Nanostructures and Nanodevices (CRANN) and Advanced Materials and BioEngineering Research Centre (AMBER), Trinity College Dublin, Dublin 2, Ireland
[3]School of Chemistry, Trinity College Dublin, Dublin 2, Ireland
*jdonegan@tcd.ie

Abstract: To achieve a feasible heat-assisted magnetic recording (HAMR) system, a near-field transducer (NFT) is necessary to strongly focus the optical field to a lateral region measuring tens of nanometres in size. An NFT must deliver sufficient power to the recording medium as well as maintain its structural integrity. The self-heating problem in the NFT causes materials failure that leads to the degradation of the hard disk drive performance. The literature reports NFT structures with physical sizes well below 1 micron which were found to be thermo-mechanically unstable at an elevated temperature. In this paper, we demonstrate an adiabatic NFT to address the central challenge of thermal engineering for a HAMR system. The NFT is formed by an isosceles triangular gold taper plasmonic waveguide with a length of 6 µm and a height of 50 nm. Our study shows that in the full optically and thermally optimized system, the NFT efficiently extracts the incident light from the waveguide core and can improve the shape of the heating source profile for data recording. The most important insight of the thermal performance is that the recording medium can be heated up to 866 K with an input power of 8.5 mW which is above the Curie temperature of the FePt film while maintaining the temperature in the NFT at 390 K without a heat spreader. A very good thermal efficiency of 5.91 is achieved also. The proposed structure is easily fabricated and can potentially reduce the NFT deformation at a high recording temperature making it suitable for practical HAMR application.

References and links

1. H. Choo, M. K. Kim, M. Staffaroni, T. J. Seok, J. Bokor, S. Cabrini, P. J. Schuck, M. C. Wu, and E. Yablonovitch, "Nanofocusing in a metal-insulator-metal gap plasmon waveguide with a three-dimensional linear taper," Nat. Photonics **6**(12), 838–843 (2012).
2. M. Schnell, P. Alonso-Gonzalez, L. Arzubiaga, F. Casanova, L. E. Hueso, A. Chuvilin, and R. Hillenbrand, "Nanofocusing of mid-infrared energy with tapered transmission lines," Nat. Photonics **5**(5), 283–287 (2011).
3. M. H. Kryder, E. C. Gage, T. W. McDaniel, W. A. Challener, R. E. Rottmayer, G. Ju, Y.-T. Hsia, and M. F. Erden, "Heat assisted magnetic recording," Proc. IEEE **96**(11), 1810–1835 (2008).
4. G. Ju, Y. Peng, E. K. C. Chang, Y. Ding, A. Q. Wu, X. Zhu, Y. Kubota, T. J. Klemmer, H. Amini, L. Gao, Z. Fan, T. Rausch, P. Subedi, M. Ma, S. Kalarickal, C. J. Rea, D. V. Dimitrov, P. W. Huang, K. Wang, X. Chen, C. Peng, W. Chen, J. W. Dykes, M. A. Seigler, E. C. Gage, R. Chantrell, and J. U. Thiele, "High Density Heat-Assisted Magnetic Recording Media and Advanced Characterization: Progress and Challenges," IEEE Trans. Magn. **51**(11), 1–9 (2015).
5. M. T. Kief and R. H. Victora, "Materials for heat-assisted magnetic recording," MRS Bull. **43**(2), 87–92 (2018).
6. N. Abadía, F. Bello, C. Zhong, P. Flanigan, D. M. McCloskey, C. Wolf, A. Krichevsky, D. Wolf, F. Zong, A. Samani, D. V. Plant, and J. F. Donegan, "Optical and thermal analysis of the light-heat conversion process employing an antenna-based hybrid plasmonic waveguide for HAMR," Opt. Express **26**(2), 1752–1765 (2018).

7. D. Weller, G. Parker, O. Mosendz, E. Champion, B. Stipe, X. B. Wang, T. Klemmer, G. P. Ju, and A. Ajan, "A HAMR Media Technology Roadmap to an Areal Density of 4 Tb/in^2," IEEE Trans. Magn. **50**(1), 1–8 (2014).
8. C. Rea, P. Subedi, H. Zhou, D. Saunders, M. Cordle, P. L. Lu, S. Granz, P. J. Czoschke, S. Hernandez, J. Jury, Y. Peng, J. U. Thiele, A. Q. Wu, G. Ju, T. Rausch, M. Seigler, and E. Gage, "High Track Pitch Capability for HAMR Recording," IEEE Trans. Magn. **53**(2), 1–7 (2017).
9. W. A. Challener, C. B. Peng, A. V. Itagi, D. Karns, W. Peng, Y. G. Peng, X. M. Yang, X. B. Zhu, N. J. Gokemeijer, Y. T. Hsia, G. Ju, R. E. Rottmayer, M. A. Seigler, and E. C. Gage, "Heat-assisted magnetic recording by a near-field transducer with efficient optical energy transfer," Nat. Photonics **3**(5), 303 (2009).
10. N. Zhou, X. F. Xu, A. T. Hammack, B. C. Stipe, K. Z. Gao, W. Scholz, and E. C. Gage, "Plasmonic near-field transducer for heat-assisted magnetic recording," Nanophotonics-Berlin **3**(3), 141–155 (2014).
11. V. Krishnamurthy, D. K. T. Ng, Z. Cen, B. Xu, and Q. Wang, "Maximizing the plasmonic near-field transducer efficiency to its limit for HAMR," J. Lightwave Technol. **34**(4), 1184–1190 (2016).
12. V. A. Zenin, A. Andryieuski, R. Malureanu, I. P. Radko, V. S. Volkov, D. K. Gramotnev, A. V. Lavrinenko, and S. I. Bozhevolnyi, "Boosting Local Field Enhancement by on-Chip Nanofocusing and Impedance-Matched Plasmonic Antennas," Nano Lett. **15**(12), 8148–8154 (2015).
13. A. Datta and X. Xu, "Comparative study of optical near-field transducers for heat-assisted magnetic recording," Opt. Eng. **56**(12), 121906 (2017).
14. B. V. Budaev and D. B. Bogy, "On the lifetime of plasmonic transducers in heat assisted magnetic recording," J. Appl. Phys. **112**(3), 034512 (2012).
15. Z. Li, W. Chen, C. Rea, M. G. Blaber, N. Zhou, H. Zhou, and H. Yin, "Head and Media Design for Curvature Reduction in Heat-Assisted Magnetic Recording," IEEE T Magn **53**(10), 1–4 (2017).
16. S. Lee, "Energy assisted magnetic recording disk drive using a distributed feedback laser," US8422342B1 (2013).
17. E. Schreck, T. Maletzky, X. Jin, Y. Zhou, K. Takano, and J. Smyth, "Directional waveguide coupler for ABS reflected light," US20120155232A1 (2012).
18. S. P. Powell, E. J. Black, T. E. Schlesinger, and J. A. Bain, "The influence of media optical properties on the efficiency of optical power delivery for heat assisted magnetic recording," J. Appl. Phys. **109**(7), 07B775 (2011).
19. G. Singh, V. Krishnamurthy, J. Pu, and Q. Wang, "Efficient Plasmonic Transducer for Nanoscale Optical Energy Transfer in Heat-Assisted Magnetic Recording," J. Lightwave Technol. **32**(17), 3074–3080 (2014).
20. V. Krishnamurthy, D. K. T. Ng, K. P. Lim, and Q. Wang, "Efficient Integrated Light-Delivery System Design for HAMR: Maximal Optical Coupling for Transducer and Nanowaveguide," IEEE Trans. Magn. **52**(2), 1–7 (2016).
21. Y. Luo, M. Chamanzar, A. Apuzzo, R. Salas-Montiel, K. N. Nguyen, S. Blaize, and A. Adibi, "On-Chip Hybrid Photonic-Plasmonic Light Concentrator for Nanofocusing in an Integrated Silicon Photonics Platform," Nano Lett. **15**(2), 849–856 (2015).
22. B. Jennings, D. McCloskey, J. Gough, T. Hoang, N. Abadía, C. Zhong, E. Karademir, A. Bradley, and J. Donegan, "Characterisation of multi-mode propagation in silicon nitride slab waveguides," J. Opt. **19**(1), 015604 (2017).
23. E. D. Palik, *Handbook of Optical Constants of Solids* (Academic, 1998).
24. E. Verhagen, L. Kuipers, and A. Polman, "Enhanced nonlinear optical effects with a tapered plasmonic waveguide," Nano Lett. **7**(2), 334–337 (2007).
25. H. Ditlbacher, N. Galler, D. M. Koller, A. Hohenau, A. Leitner, F. R. Aussenegg, and J. R. Krenn, "Coupling dielectric waveguide modes to surface plasmon polaritons," Opt. Express **16**(14), 10455–10464 (2008).
26. R. G. Hobbs, V. R. Manfrinato, Y. Yang, S. A. Goodman, L. Zhang, E. A. Stach, and K. K. Berggren, "High-energy surface and volume plasmons in nanopatterned sub-10 nm aluminum nanostructures," Nano Lett. **16**(7), 4149–4157 (2016).
27. X. Fan, W. Zheng, and D. J. Singh, "Light scattering and surface plasmons on small spherical particles," Light Sci. Appl. **3**(6), e179 (2014).
28. R. G. Hobbs, Y. Yang, A. Fallahi, P. D. Keathley, E. De Leo, F. X. Kärtner, W. S. Graves, and K. K. Berggren, "High-Yield, Ultrafast, Surface Plasmon-Enhanced, Au Nanorod Optical Field Electron Emitter Arrays," ACS Nano **8**(11), 11474–11482 (2014).
29. C. Birleanu, M. Pustan, V. Merie, R. Muller, R. Voicu, A. Baracu, and S. Craciun, "Temperature effect on the mechanical properties of gold nano films with different thickness," IOP Con. Mat. Sci. **147**(1), 012021 (2016).
30. A. Krichevsky, C. Wolf, F. Bello, K. Ballantine, J. Donegan, D. McCloskey, "Method and system for reducing undesirable reflections in a HAMR write apparatus," US9484051B1 (2016).
31. B. Dieny, M. Chshiev, B. Charles, N. Strelkov, A. Truong, O. Fruchart, A. Hallal, J. Wang, Y. K. Takahashi, and T. Mizuno, "Impact of intergrain spin transfer torques due to huge thermal gradients on the performance of heat assisted magnetic recording," arXiv preprint arXiv:1712.03302 (2017).
32. W. A. Challener and A. V. Itagi, "Near-field optics for heat-assisted magnetic recording (experiment, theory, and modeling)," Modern Aspects of Electrochemistry **44**, 53– 111 (2009).
33. A. Datta and X. Xu, "Improved near-field transducer design for heat-assisted magnetic recording," IEEE Trans. Magn **52**(12), 1–6 (2016).
34. N. Zhou, E. C. Kinzel, and X. Xu, "Nanoscale ridge aperture as near-field transducer for heat-assisted magnetic recording," Appl. Opt. **50**(31), G42–G46 (2011).

35. X. Shi and L. Hesselink, "Mechanisms for enhancing power throughput from planar nano-apertures for near-field optical data storage," J. Appl. Phys. **41**(3), 1632–1635 (2002).
36. T. Matsumoto, F. Akagi, M. Mochizuki, H. Miyamoto, and B. Stipe, "Integrated head design using a nanobeak antenna for thermally assisted magnetic recording," Opt. Express **20**(17), 18946–18954 (2012).
37. T. Matsumoto, Y. Anzai, T. Shintani, K. Nakamura, and T. Nishida, "Writing 40 nm marks by using a beaked metallic plate near-field optical probe," Opt. Lett. **31**(2), 259–261 (2006).

1. Introduction

Nanofocusing – the process of concentrating light to dimensions below the conventional diffraction limit – has been utilized in a wide variety of practical applications [1, 2], and is currently an enabling technology for the development of a data storage process known as heat-assisted magnetic recording (HAMR) [3]. The latest high-capacity hard disk drives (HDDs) from Seagate and Western Digital Corporation have areal densities up to 1.4 Tb/in^2 [4–6]. Studies have shown that HAMR may achieve areal memory density up to 4 Tb/in^2 or even 5 Tb/in^2 in the next few years [7]. HAMR is projected to increase storage capabilities roughly 10-fold above the current perpendicular magnetic recording (PMR) technology. However, due to the reliability issues with the NFT, HAMR is still not yet ready for full-scale commercial implementation [8]. HAMR operates by nonradiative coupling of energy from a plasmonic element to the surface of the ferromagnetic recording medium to raise the local temperature, which reduces the coercivity of the material. When placed in the field of a writing magnet, the magnetization state of the illuminated area can be altered without affecting its surroundings, creating a magnetic bit. Thus, the memory density is dependent on the degree of spatial confinement in the optical nanofocusing process. Although heating the magnetic material can be done through other means, the optical method is the most common, particularly with a NIR (near infrared) diode laser coupled to a dielectric waveguide integrated with a plasmonic element known as a near-field transducer (NFT) at the air-bearing surface (ABS).

When designing a nanofocusing element for commercial applications, the NFT's ability to harvest incident light while maintaining its structural integrity under strong optical intensities is of critical importance [9–11]. While there has been a significant amount of research on optimizing nanofocusing in terms of spatial confinement (for example, achieving a spot-size diameter of 60 nm in a tapered transition line [2]) and field concentration (for example, a theoretical intensity enhancement of 12000 × in a tapered stripe nanofocuser [12]), these papers are typically concerned neither with damage imparted to the optical structures during use, nor with the need for the nanofocusing element to efficiently extract all of the incident power. For the first concern, concentrating such a large amount of radiation in such a small space can cause the nanostructures to deform, or at least alter the material's thermal, optical, and electrical properties in a deleterious manner. The literature reported that the temperature can reach as high as 721 K in a 150 nm long triangular antenna when the nanofocusing process occurs [13] – the structural integrity of the nanofocusing element needs to be maintained for repeated use for thousands of hours in a commercial system [14]. For the second concern, any uncoupled incident light can illuminate and heat the wrong part of the magnetic medium as well as broaden the heating source profile, potentially causing a bit to be lost or overwrite the bits on the disc which will increase the bit error rate [15]. Moreover, in certain instances, light reflected from the end of the waveguide can destabilise the light source, reducing performance of HAMR [16]. A good coupling system is desired to improve the light energy distribution at the media interface with the ABS which contributes to a more controlled thermal gradient at the media for higher recording density [17].

In this study, we demonstrate an NFT structure, a long tapered device which can indeed couple light efficiently and which has the potential to be exploited in HAMR systems. This paper combines experimental, simulation, and theoretical techniques to characterize a particular NFT composed of an evanescently coupled plasmonic taper [10, 18–20], designed to address the thermally induced device deformation issue that hinder HAMR development.

In an effort to maximize the dielectric waveguide to plasmonic waveguide coupling efficiency, the length of the NFT is chosen to be two orders of magnitude longer than what is seen in similar devices [21]. This particular design can minimize the optical energy in the dielectric waveguide core meanwhile maximizing the energy in the NFT. This creates a favourable thermal source profile for data storage. Moreover, the heat can be effectively dissipated in a large piece of metal during the recording process, resulting in a lower operating temperature for the write head. Optical and thermal analysis have been applied to the system to achieve the required temperature and spot size in the recording medium.

2. NFT design

The evanescent coupling system of interest is shown in Fig. 1. The dielectric waveguide consists of a 180 nm thick LPCVD deposited silicon nitride (Si_3N_4) core on a 2 µm thermally grown silicon dioxide (SiO_2) layer on Silicon (Si-Mat). This structure can support only one transverse magnetic (TM) and one transverse electric (TE) mode at the free space wavelength of $\lambda_0 = 850$ nm [22]. The evanescent coupling between the core Si_3N_4 (refractive index = 2.02) waveguide and the NFT occurs in the presence of another dielectric layer with a smaller index than the core, here chosen to be SiO_2 (refractive index = 1.45). This spacer layer of SiO_2 has a thickness of $t_s = 188$ nm used to match the effective refractive index of the photonic and the plasmonic modes. The NFT is formed by an isosceles triangular gold (Au) plasmonic waveguide (50 nm thick) which is situated on the SiO_2 layer. The top cladding is air. A diode laser with a wavelength of 850 nm is used to illuminate the NFT from a trench which is 4 mm away (much further than depicted in Fig. 1 which is not to scale). The evanescent coupling can be understood in the context of momentum conservation, as the effective indices of the photonic and plasmonic modes (corresponding to the momentum of the light) have to match for the process to occur. The coupled mode is a hybridization of the photonic mode and the plasmonic mode, which propagates towards the tip of the taper to be concentrated there. Because plasmonic modes are always excited by TM polarized wave, the light source will be TM polarized for the entire work.
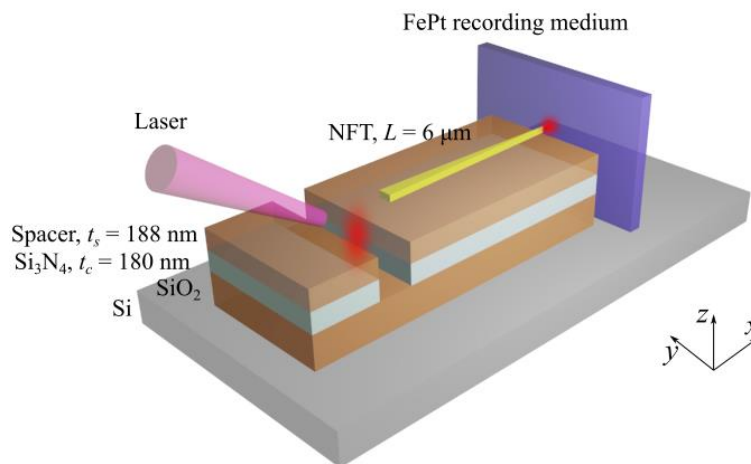

Fig. 1. Schematic diagram of the proposed evanescent coupling system. It consists of a 180 nm Si_3N_4 dielectric waveguide with a 188 nm SiO_2 spacer layer. The propagating photonic mode in the Si_3N_4 waveguide is excited via an opening trench which will couple to the plasmonic mode in the NFT. The position of the FePt recording medium is also shown.

2.1 Optical analysis

Figure 2(a) shows the monochromatic 3-D finite element method simulations for the optical analysis, simulated using the commercial software COMSOL. The complex permittivity of

Au used in the calculations was obtained from Palik [23]. The systems under study will be characterized by three parameters: the field intensity enhancement (i.e., the degree of nanofocusing), the coupling efficiency (amount of light coupled out from the core layer) and the coupling length (the distance between peaks in the field oscillations below the NFT). These three things can be clearly seen in Figs. 2(a)-2(j), which are models of the electric field intensity in different planes of the system using the optimized thickness parameters. Both a tapered structure [Figs. 2(a)-2(e)] and a rectangular structure (Figs. 2(f)-2(j)) were simulated to visually see the adiabatic nanofocusing process occurring in a tapered geometry rather than a uniform structure. Whenever a taper and rectangle are discussed in tandem, they will have the same length L. The width of the rectangle and the starting width of the NFT will always be 1 μm; the width of the tapered NFT at the tip is 50 nm. The simulations were performed with the custom mesh setting, where the maximum mesh size is 170 nm ($\lambda_0/5$) and minimum mesh size is 1 nm.
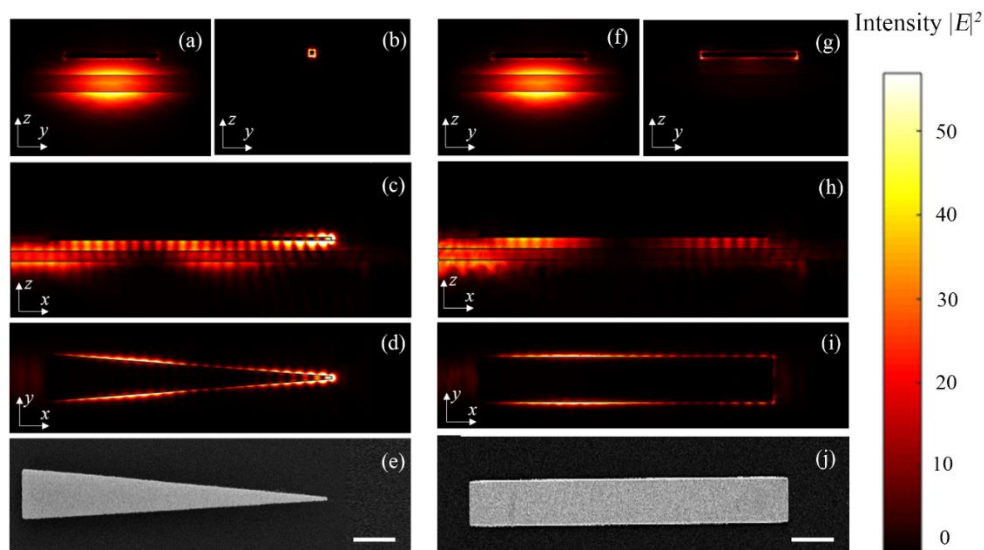

Fig. 2. Optical 3-D simulations of the electric field distribution in the NFT with a tapered Au plasmonic waveguide (a)-(d) and a rectangular Au strip waveguide (f)-(i): (a), electric field at the start of the Au taper; (b), electric field at the tip of the Au taper; (c) the side view of the Au taper in the x-z plane shows mode beating; (d), top view of the Au taper shows the nanofocusing process. The same description can be applied to panels (f) – (i) which are simulated results for an Au rectangular strip acting as a reference sample, the difference being that the nanofocusing effect doesn't appear at the end of the rectangle. Light propagates in the x direction in all figures. The colour bar shows the strength of the intensity which is normalized with the average intensity in the input port of the Si_3N_4 core layer. Panels (e) and (j) show SEM images of the fabricated taper and rectangular test structures. The scale bar is 1 μm and applies to all panels.

The first three rows of the simulated results are maps of the electric field intensity at different cross-sections, Figs. 2(a)-2(e), with the light propagating in the x direction. The top row is in the y-z plane; the left panel [Fig. 2(a)] is at the start, which is dominated by the photonic TM mode used to excite the system, and the right panel [Fig. 2(b)] is at the tip of the NFT, which is dominated by the focused plasmonic mode. The slab waveguide confines the light along the z direction and the lateral size of the Au taper can confine the light in the y direction. The cross-section of the tip of the NFT is 50 nm $\times$ 50 nm in size in the y-z plane, the SPP can be highly confined in this region. The side view in the x-z plane [Fig. 2(c)] shows the intensity in this plane which shows feature of mode beating. The third row [x-y plane, Fig. 2(d)] shows the nanofocusing process, with the intensity becoming very large at the tip of the

NFT [24], but not at the end of the rectangle [Fig. 2(i)], as expected. In both cases, mode beating is observed, with the tapered case having a shorter coupling length. Also notable is the fact that more light is concentrated in the spacer layer when the structure is tapered, which indicates a better coupling efficiency. The bottom row contains SEM images of the fabricated NFT (Fig. 2(e)) and rectangle (Fig. 2(j)) samples corresponding to the ones simulated above.

In Fig. 3(a), the intensity distribution in the spacer layer of the tapered NFT (red curve) and the rectangular waveguide (black curve) as a function of position for an Au layer that extends from $x = 1$ to 7 μm ($L = 6$ μm) is plotted. Each curve is normalized against its own highest value. The intensity is collected along the centre of the SiO_2 spacer layer. Both curves in Fig. 3(a) exhibit beat-like behavior. The higher frequency oscillation is due to the plasmonic mode: it was found that the peak-to-peak separation is nearly identical to half of the plasmonic wavelength ($\lambda_{spp} = 267$ nm). The lower frequency oscillation is due to the mode beating between the plasmonic mode and the photonic mode: it can be seen that the normalized intensity near the end of the taper (for 5 μm $< x < 7$ μm) is higher than in the same range of the rectangle which demonstrates that the Au NFT can extract power from the Si_3N_4 core more efficiently than the Au rectangular strip because of the strong mode beating in the tip. The rectangle has a shorter coupling length due to the smaller value of effective refractive index of the plasmonic mode in a uniform structure compared with a tapered triangle.

The mode beating-induced field intensity enhancement factor Π_{NFT} in the NFT is calculated by using the absolute square of the electric field in the output port divided by the input port of the NFT. Figure 3(b) shows the field intensity enhancement factor in the Au NFT as the length L varies from 100 nm to 25 μm in steps of 100 nm. The curves exhibit exponential decay as the length increases (due to ohmic losses in the metal), as well as oscillations induced by mode beating between the photonic and plasmonic modes.
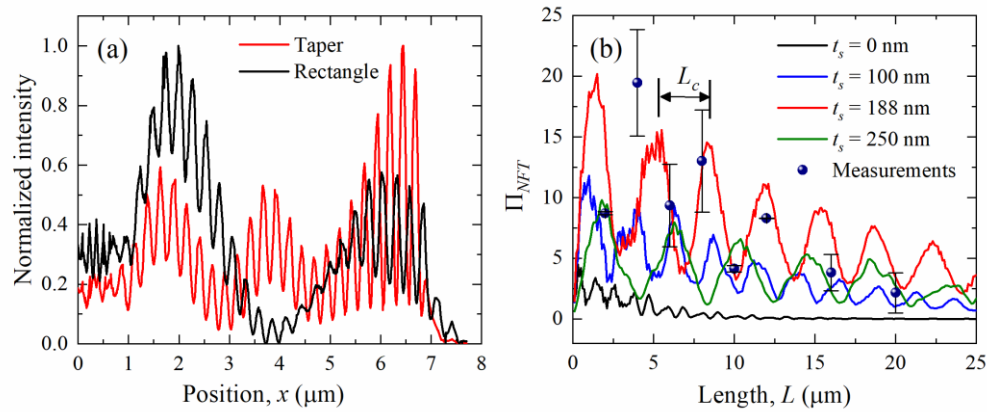

Fig. 3. (a) The normalized intensity distribution in the spacer layer of the tapered and rectangular waveguides along the light propagation direction. (b) The field intensity enhancement factor in the NFT at different values for the spacer layer thickness (t_s). The ratio shown is the output port of the Au layer against the input port. The curves exhibit the expected exponential decay as well as oscillations corresponding to the coupling length (labelled L_c). The experimental data from the optical far-field measurements for the $t_s = 188$ nm samples are overlapped with the simulation.

The distance between the peaks of the oscillations curves seen in Fig. 3(b) is known as the coupling length L_c [25], formally defined as:

$$L_c = \frac{\lambda_0}{2} \left| \frac{1}{n'_p - n'_d} \right| \tag{1}$$

where n'_p and n'_d are the effective indices of the particular plasmonic and photonic modes that have been coupled, respectively. In our evanescent coupling system, these are $n'_p = 1.71$ and $n'_d = 1.59$, corresponding to a theoretical coupling length of $L_c = 3.54$ µm, the simulated coupling length [shown in Fig. 3(b)] is $L_c = 3.30$ µm.

When the spacer layer is at its optimized thickness (where $t_s = 188$ nm), the value of Π_{NFT} is highest, which will result in efficient nanofocusing at the NFT tip. The curves at other thicknesses ($t_s = 0$ nm, 188 nm and 250 nm) demonstrate the importance of correctly designing the spacer layer in the previous steps. They show the reduction of the optical field enhancement when $t_s <$ or > 188 nm. When the taper is short, very high enhancement factors can be achieved (Π_{NFT} is found to be ~20 when $L = 2$ µm). Selecting a length value where the curve is at a maximum allows the use a very long taper ($L > 5$ µm) for increased coupling efficiency while still maintaining the nanofocusing effect. For example, a field enhancement factor of 10 can still be achieved when the length of the taper is 15 µm.

The optical performance of the fabricated devices was characterized with an optical far-field measurement. The wafer layer structure used in this work is shown in Fig. 1. The core is a layer of Si_3N_4 on a 2 µm thick SiO_2 layer on a silicon substrate. The thickness of the Si_3N_4 is 180 nm which only supports the fundamental TM and TE modes at the input light wavelength of $\lambda_0 = 850$ nm. A 188 nm thick SiO_2 spacer layer was deposited directly on the Si_3N_4 layer through a magnetron sputtering system. The flat edge opening for coupling of the incident light was fabricated by patterning a rectangular trench through a UV lithography system. The Au taper was patterned by electron beam lithography (EBL). Since the dimensions of the NFT varied from 24 µm (the largest L value) to 50 nm (the nominal width of the tip and the layer thickness) the EBL process had to be carefully optimized [26]. We use a Carl Zeiss Electron Beam Lithography SEM – Supra 40 system to do the fabrication, the finest feature is 50 nm is our optimized recipe, and we made 12 samples for each length to test the repeatability of the fabrication and the variation of the length for the tapers is less than 2.5%. Optical far-field measurements were conducted to experimentally observe how the Π_{NFT} value varies with the length of the taper as shown in Fig. 4.
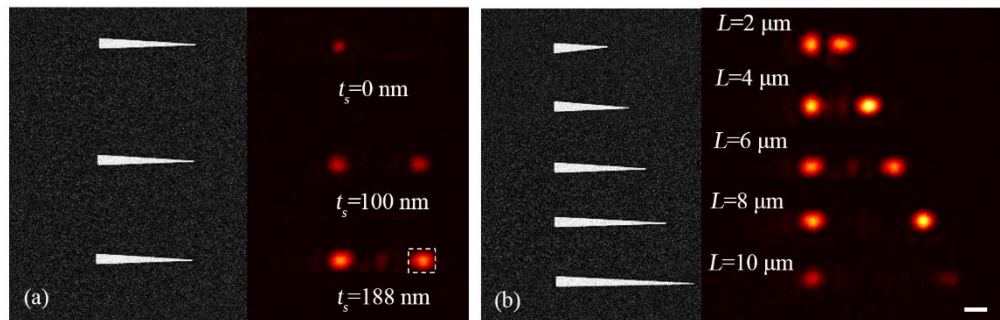

Fig. 4. Left side of panel: SEM images; right side of panel: corresponding CCD images from the optical far-field measurements. (a) Measured results of the $L = 6$ µm sample with a variable spacer layer thickness ($t_s = 0$ nm, 100 nm, and 188 nm from top to bottom). (b) Measured results of the samples with an optimal spacer layer (188 nm), at different lengths. The light is incident from the left side. The scale bar is 2 µm for all four images. Note that the structures were much farther apart than this on the actual sample (30 µm).

The CCD images were captured with a 40 × objective lens (NA = 0.6) with a long working distance. The power at the output of the taper are obtained by integrating the counts in a 30 × 30 pixel square in the CCD images, which is shown in the dashed-white square in Fig. 4(a). The input power are obtained by integrating the counts in the background of the CCD images, where they do not show field enhancement. The samples were characterized by coupling the TM-like wave to the NFT from the opening trench. Figure 4(a) shows the

measured results of 3 tapers with the length of 6 µm, the thickness of the spacer layers are $t_s = 0$ nm, 100 nm and 188 nm, respectively. The discontinuity of the effective refractive index between the photonic core and Au NFT will result in scattering when the evanescent field couples to the Au taper and excites the plasmonic mode, which will result in bright spots at the start (left end) of the structures [27]. The light is barely able to couple into the Au taper if there is no spacer layer ($t_s = 0$) and no enhancement appears in the tip because of the loss in the metal, which shows a good agreement with the discussion from Fig. 3(b) (the NFT with 188 nm spacer layer has the highest intensity enhancement factor). The intensity enhancement factor in the tip of the taper with a 188 nm spacer layer is ~7 times higher than with a 100 nm spacer layer.

We can visually see the mode beat behaviour from Fig. 4(b). Apart from the 10 micron case, all the tapers show a strong enhancement and this should be compared with the modelling results in Fig. 3(b). A taper length of 10 microns in both the modelling and the experimental results shows a small enhancement due to the mode beating effect. The experimental data after normalizing with the input of the taper is overlapped with the simulated data which can be seen in Fig. 3(b). The optical field enhancement happens when L is an integral multiple of the coupling length. $L = 8$ µm has a higher optical field enhancement than $L = 6$ µm, but $L = 8$ µm is not an optimal length for the thermal performance. Looking at Fig. 3(b), we can see that $L = 10$ µm is a local minimum and in Fig. 4(b), we see this clearly in the experimental results. The experimental data show better agreement with the theory when the tapers are long. The Ti adhesion layer can cause some error (it was not included as a layer in the simulations), but the effect is generally small in structures with tens of micrometres in length [28]. Note also that the measurement and theory are different in the sense that the experimental results can only collect light scattered at the tip over a specific solid angle, while the simulations can collect all of the scattered light. Nevertheless, the data shows reasonable agreement and validates our approach. Although the 6 micron taper does not have the largest enhancement, we have chosen this particular length for ease of measurement in the results in Fig. 4 and also as a length that will effectively reduce the power remaining in the core at its end.

Underneath the NFT, the intensity needs to be minimized at the ends of the lower dielectric layers (SiO_2 and Si_3N_4) when used in a HAMR system to prevent interference with the magnetic medium or the light source as well as stablize the thermal gradient in the FePt recording medium. As before, optimizing the spacer layer thickness gives higher-intensity enhancement in the NFT, but the goal is to reduce the intensity in the core layer to a minimum. Table 1 lists the intensity enhancement factor in the NFT and percentage of the power contained in three different simulation domains as the thickness of the spacer layer is varied.

Table 1. Intensity enhancement in the NFT and percentage of the intensity distribution in different simulation domains for a 6 µm long NFT when the thickness of the spacer layer is varied. In each case, the excess intensity is in the air or substrate layer.

Thickness of the spacer, t_s (nm)	Π_{NFT}	Total intensity in simulation domains		
		NFT	Spacer layer	Core layer
0	0.8	4.04%	0	12.7%
100	7.0	17.8%	10.6%	19.2%
188	16	57.8%	23.7%	2.90%

The 6 µm long taper with spacer layer thickness of 188 nm design can achieve the best figure of merit when considering both the optical and thermal performances. 57.8% of the light is now coupled to the NFT when the thickness of the spacer layer is optimized ($t_s = 188$ nm) and the corresponding $\Pi_{NFT} = 16$ which is the highest value from our studies. A lower value of 17.8% is achieved when $t_s = 100$ nm, it results in a lower $\Pi_{NFT} = 7$. The percentage of power in the spacer layer that has been transferred from the core layer to the NFT, is 23.7% and 10.6% when $t_s = 188$ nm and $t_s = 100$ nm, respectively; this shows that the spacer layer

with an optimal thickness can effectively increase the coupling efficiency between the plasmonic mode and the photonic mode. Any light in the core layer will cause potential miswriting on the recording medium, it needs to be minimized (only 2.90% remaining in the core layer when t_s = 188 nm for taper length of 6 μm). By properly designing the length of the NFT, a local minimum intensity in the dielectric layer (spacer layer and core layer) and a maximum in the NFT tip can be achieved. The light energy distribution at the media interface contributes to an improved heating source profile for date writing as well as a more controlled thermal gradient at the media for higher recording density, the detailed analysis of the heat distribution in the recording medium as a function of the taper length will be described in the thermal analysis part.

2.2 Thermal analysis

Failure of the NFT is the main difficulty holding back the introduction of HAMR. With temperature rises of ~100 K in the NFT, the hardness of Au films may be reduced by half due to the self-heating problem and adhesion force changes can significantly increase film degradation [29]. Au films generally use a Ti or Cr adhesion layer to promote film stability and to minimize the de-wetting process. Ideally, we need to heat up the recording medium above 650 K and keep the temperature in the Au NFT below 450 K. It is vital to have a good model which accurately predicts the thermal behaviour of this NFT. For the thermal analysis, we extracted the resistive heating losses in the entire domain from the optical simulation and then use values of the resistive heating losses as the heating source to solve the steady state heat equation to calculate the temperature distribution in the coupled system [6].
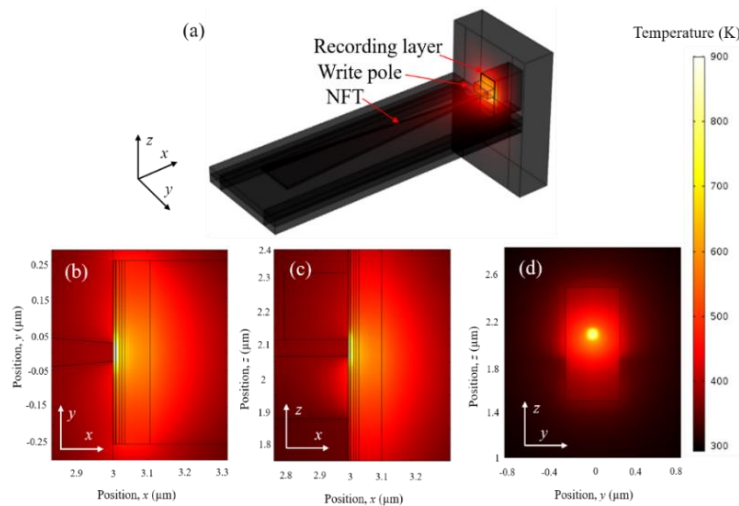

Fig. 5. Thermal simulation of the NFT with an evanescent coupling mechanism. (a) COMSOL model for the 6 μm long tapered NFT with a recording medium. The recording medium is consisting of a 9 nm FePt layer, 72 nm Cu heat sink on a SiO$_2$ substrate. There is a 2.5 nm air-gap between the Au NFT and the recording medium. Capping layer and contaminants such as Carbon form the Carbon overcoat (COC) layer are also present in the thermal model. (b) The cross-section view of the heat distribution in the centre of the x-z plane. (c) The top-down view of the heat distribution in the interface plane of the SiO$_2$ spacer layer and the Au NFT in the x-y plane, the hot spot shows in the ABS interface. (d) Cross-section view on the recording medium in the y-z plane, it is the cross-track and down-track directions, the recording layer is locally heated up. The highest temperature on the recording medium can reach 866 K with an 8.5 mW input power in the Si$_3$N$_4$ core.

Figure 5 shows the thermal simulation of the NFT with an evanescent coupling mechanism. The COMSOL model of the 6 μm long tapered NFT with a recording medium can be seen in Fig. 5(a). The recording medium is consisting of a 9 nm FePt layer, 72 nm Cu

heat sink on a SiO₂ substrate. There is a 2.5 nm air-gap between the Au NFT and the recording medium. Capping layer and contaminants such as Carbon form the Carbon overcoat (COC) layer are also present in the thermal model. More detail of the recording layer are reported in our previous publication [6]. Figure 5(b) shows the cross-section view of the heat distribution along the central of the *x-z* plane. It can be seen that the heat is highly concentrated at the tip of the NFT. Figure 5(c) is the top-down view of the heat distribution in the interface of the SiO₂ spacer layer and the Au NFT along the *x-y* plane. It shows that the recording layer is locally heated up to 866 K. Figure 5(d) indicates the cross-section view on the recording medium along the *y-z* plane. The target hotspot size in the magnetic medium is 50 nm × 50 nm in this project. The minimum spot size from the thermal simulation is 50 nm × 30 nm which can be seen in Fig. 7(a). The project was carried out in collaboration with Western Digital. A hotspot with 50 nm × 50 nm in size, with areal density in a 2.5 inch hard disk drive of 0.26 Tb/in^2 was specified. Our design with a 50 nm × 30 nm spot size will result in an areal density of 0.43 Tb/in^2. Our previous work showed that the hot spot is adjustable by properly designing the cross-section of the NFT [6]. To achieve an areal density of 4 Tb/in^2 will require an NFT of much smaller size.
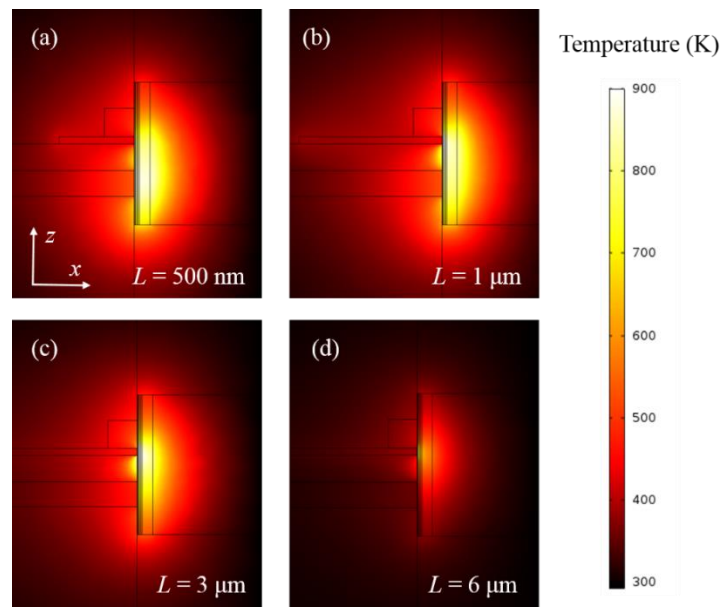

Fig. 6. The temperature distribution in the recording medium as a function of the taper length. Panels (a) to (d) are the tapers with the length of 500 nm, 1 μm, 3 μm and 6 μm respectively. It shows that a longer taper can effectively couple the light from the waveguide core to the Au NFT, which can improve the profile of the thermal spot in the recording medium.

The highest temperature on the recording medium can reach 866 K with an 8.5 mW input power in the Si₃N₄ waveguide. In our proposed long tapered NFT, the highest temperature in the NFT is 390 K owing to the heat dissipation in a large piece of Au. A similar design used a heat spreader above the Au NFT to maintain the temperature in the Au below 450 K to avoid deformation under an elevated temperature [6]. The long tapered NFT can work without the use of a heat spreader and manufactured with a simple fabrication process. The heat spreader would increase the difficulty in fabricating the device. The long NFT in our paper is a simple structure and it is a feasible design to be fabricated via a standard EBL process.

The uncoupled light remaining in the Si₃N₄ core and SiO₂ spacer layer will heat the recording medium below the NFT which will broaden the heating source reducing the maximum areal density capacity of the HAMR system [15]. In order to obtain the desired performance, a high coupling efficiency is desired between the waveguide and the NFT. Our

previous work showed an antireflective mechanism can control the back reflection in the HAMR system improving the performance of the NFT [30]. In addition, rectangular waveguides will also be necessary to make the dielectric waveguide single mode. A long taper in this paper can couple sufficient light from the guiding dielectric core layer to the Au NFT which in turn improves the heating source profile for data recording. The heat distribution in the recording medium as a function of the taper length is plotted in Fig. 6. The result shows that a longer taper can produce a smaller thermal spot in the recording medium which can effectivity heat up the desired region on the recording medium.

From a thermal point of view, the media is designed to avoid a lateral spread of the heat and in contrast, fast thermal dissipation towards the underlying substrate is preferred. This is naturally achieved through the anisotropic properties of FePt due to the columnar grain growth. A heat sink layer of Cu (72 nm) is used underneath the recording layer to increase the downwards vertical heat flow throughout the media, which is beneficial to achieve a high thermal gradient in the recording media [31]. Figure 7(a) is the zoomed-in temperature map on the surface of the FePt recording layer from Fig. 5(d). The contour plot is overlapped with the temperature map which shows the thermal gradients in the cross-track and the down-track directions. The temperature decreases gradually as the position is moving away from the tip of the Au NFT. The FePt recording layer can be heated up locally above 800 K with 50 nm $\times$ 30 nm in size. A highest temperature of 866 K is achieved in the centre of the hot-spot. The anti-symmetric feature of the hot spot is due to the presence of the write pole. Panel (b) and (c) are the thermal gradient graphs of the cross-track and down-track directions respectively. The magnetic field intensity drops rapidly with the distance from the write pole, the thermal gradient is measured in the FePt layer which is 9 nm away from the write pole.
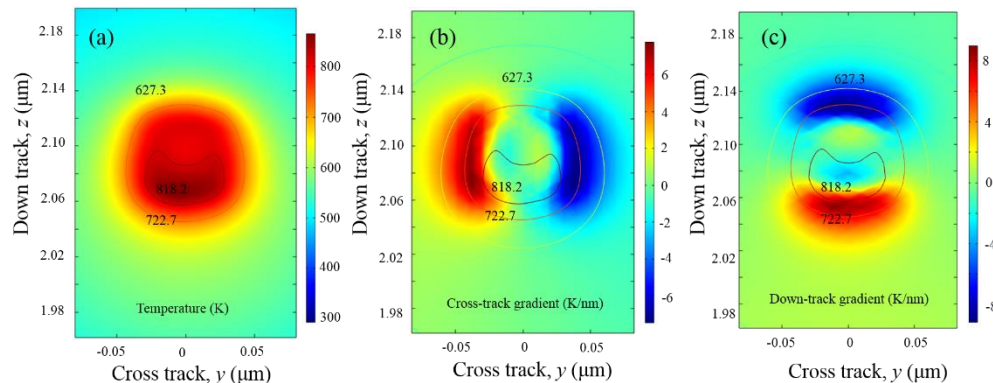

Fig. 7. (a) Zoomed-in temperature map on the surface of the FePt recording layer. The contour plot is overlapped with the temperature map which shows the thermal gradients in the cross-track and the down-track directions. The y axis represents the cross-track direction and the z axis is down-track. Panel (b) and (c) are the thermal gradient graphs of the cross-track and down-track respectively.

3. Discussion

For a properly functioning HAMR system, the design of the NFT to allow nanofocusing while maintaining the thermo-mechanical integrity of the NFT is crucial to the performance of the entire system. Table 2 summarize the thermal figures of merit for different recently proposed NFT designs from the literature. There are a variety of NFT designs for HAMR, such as triangle antenna [32], antenna based hybrid photonic-plasmonic waveguide [6], lollipop antenna [9], E antenna [33], bowtie aperture [34], C-aperture [35], nanobeak [36, 37]. We summarize the first three types of NFTs only which are relevant to our long tapered NFT. For an NFT design, the temperature of the recording medium needs to be raised to above the Curie temperature while maintaining the temperature rise in the NFT to be as low as possible.

To prevent thermal damage to the NFT, it is important to evaluate its temperature evolution during the heating process. Table 2 shows the steady state thermal efficiency figures of merit. The thermal efficiency is taken as the ratio of peak temperature rise in the recording medium to the peak temperature rise in the NFT ($\frac{\Delta T_{medium}}{\Delta T_{NFT}}$). A highest thermal efficiency of 5.91 is achieved in our adiabatic hybrid NFT design since heat can quickly diffuse over a large area of the metal taper. A similar performance with a thermal efficiency of 3.8 was achieved in our previous antenna based hybrid NFT. However, a heat spreader is necessary to cool down the NFT in that design. The NFTs in the triangle and lollipop designs get very hot when heating up the recording medium. Without the use of any heat dissipation elements, the highest temperature in the NFTs are 721 K and 625 K respectively which induces a low thermal efficiency (0.87 and 1.24 respectively). The temperature rise in the recording medium per unit input power is another parameter to describe how efficient the system is. A 8.5 mW input power is needed in our long NFT to heat up the recording medium to a sufficiently high temperature which results in a relatively low temperature rise per unit input power, 67.3 K/mW is achieved. Compared to other designs that use a 3 to 5 mW input power (maximum value of 109.3 K/mW in the antenna based hybrid NFT), there is a larger energy waste in a long taper. However, the simple taper NFT can keep its integrity under an elevated recording temperature without the using of a heat spreader.

Table 2. Steady state thermal figures of merit for the triangle and antenna based NFTs

NFTs design	Length (µm)	T_{NFT} (K)	T_{medium} (K)	$\frac{\Delta T_{medium}}{\Delta T_{NFT}}$	Thermal spot size	Temp. rise per unit power (K/mW)	Thermal gradient (K/nm)	
							Cross-track	Down-track
Triangle antenna	0.15	721	665	0.87	63 nm × 76 nm	74.5	3.5	4.6
Lollipop antenna	0.09	625	705	1.24	65 nm × 71 nm	82.4	3.7	3.14
Antenna based hybrid NFT	0.33	403	813	3.80	50 nm × 50 nm	109.3	14.1	15.1
Adiabatic hybrid NFT	6	390	866	5.91	50 nm × 30 nm	67.3	9.36	10.4

The thermal gradient can be described as the temperature change per unit length on the recording medium. A high thermal gradient in the recording medium helps to ensure that the thermal spot generated in the medium is comparable to the optical spot, rather than a smeared out spot that will inadvertently write on the adjacent magnetic domain. The thermal gradients are expressed for both the down-track and the cross-track directions. The cross-track gradient is related to the track density while the down-track gradient determines the linear density of data [13]. Higher thermal gradients are preferred in the recording medium, which will eliminate long thermal tails. A capping layer with high thermal conductivity is present in the recording medium which will inevitably decrease the thermal gradient in the FePt recording medium. A lower thermal conductivity of the capping layer is chosen for the capping (5 W/m/K) than our previous thermal model (20 W/m/K) to obtain a compatible thermal gradient in the FePt recording layer. The thermal gradient along in the cross-track and down-track directions of the recording medium is ~10 K/nm for either the antenna hybrid based NFT or the adiabatic hybrid NFT, the high thermal gradient is obtained in these two evanescent coupling system mainly attribute to the Cu heat sink layer which has a high thermal conductivity was used in the recording medium. A layer of MgO and Amorphous underlayer were present in our thermal model which can further increase the thermal gradient. The absence of heat sink layer in the triangle and lollipop antennae NFTs results in a low

thermal gradient which is < 5 K/nm, moreover, without dissipating the heat effectively, the entire NFTs work as heating sources which cannot heat the recording medium locally. An increase in the thermal gradient can be achieved by replacing low thermal conductivity heat sink and underlayer materials with high thermal conductivity materials [15].

4. Conclusions

In conclusion, we theoretically and experimentally demonstrated an adiabatic near-field transducer (NFT) that could effectively dissipate heat to protect its structural integrity during the nanofocusing process. In the optical analysis, an optimal thickness of 188 nm SiO_2 spacer layer can effectively couple 57.8% of the light in a 180 nm thick Si_3N_4 core waveguide to a tapered Au NFT producing a minimum optical power in the guiding dielectric waveguide. This is beneficial to improve the shape of the thermal source profile on the recording medium. An evanescent coupling system with hybrid waveguides was used, the mode beating between the plasmonic mode and the photonic mode contributed to an enhancement factor of $16 \times$ for an Au taper 6 μm in length. The thermal analysis indicates that a 6 μm long NFT can effectively dissipate the heat in it without the using of a heat spreader. Results show that with using an 8.5 mW input laser, the recording medium can be heated up to 866 K and meanwhile the highest temperature in the NFT remains at 390 K, which can ensure its structural integrity when it is working in a HAMR device. The systematic study of the optimal designed evanescent coupling system provides helpful insights about the operational mechanism and performance as well as the strategies for the design of an efficient NFT in a HAMR system. Such a long taper should be much more thermo-mechanically robust, a key problem that limits the present HAMR system employing NFTs with sub-micron dimensions.

Funding